Unveiling Double A-site Cation Perovskite-Inspired Materials: From 0D-$Cs_3Bi_2I_9$ to 2D-$Cs_2AgBi_2I_9$ with Enhanced Charge Transport

Mozakkar Hossain[ǂa,b], Kuntal Singh[ǂa], Ankita Narwal[c], Md Sariful Sheikh[a], Sandeep K Reddy[d], Kiran Vankayala[e], Asha Singh[f], Saleem Khan[f,g], Salahuddin Khan[f,g], Praveen Kumar Velpula[h], Manohar Chirumamilla[i,j], Sharma S. R. K. C. Yamijala[c,k,l,m], G. Krishnamurthy Grandhi[n], Paola Vivo[n], K. D. M. Rao[a]*

[a] *School of Applied & Interdisciplinary Sciences, Indian Association for the Cultivation of Science, Jadavpur, Kolkata 700032, India, E-mail: saiskdmrao@iacs.res.in (K. D. M. R.).*

[b] *Present Address: Department of Mechanical and Aerospace Engineering, University of California, Los Angeles, California 90095, USA*

[c] *Department of Chemistry, Indian Institute of Technology Madras, Chennai 600036, India*

[d] *Centre for Computational and Data Science, Indian Institute of Technology Kharagpur, Kharagpur, West Bengal, 721302, India*

[e] *Department of Chemistry, Birla Institute of Technology and Science (BITS) Pilani, K. K. Birla Goa Campus, Zuarinagar, Goa 403726, India*

[f] *Raja Ramanna Centre for Advanced Technology, Indore (M.P.) 452013*

[g] *Homi Bhabha National Institute, Mumbai*

[h] *UGC-DAE Consortium for Scientific Research, University Campus, Khandwa Road, Indore (M.P.) 452001.*

[i] *Department of Materials and Production, Aalborg University, Skjernvej 4A, Aalborg 9220, Denmark*

[j] *Institute of Optical and Electronic Materials, Hamburg University of Technology, Eissendorfer Strasse 38, Hamburg 21073, Germany*

[k] *Centre for Quantum Information, Communication, and Computing, Indian Institute of Technology Madras, Chennai 600036, India*

[l] *Centre for Atomistic Modelling and Materials Design, Indian Institute of Technology Madras, Chennai 600036, India*

[m] *Centre for Molecular Materials and Functions, Indian Institute of Technology Madras, Chennai 600036, India*

[n] *Hybrid Solar Cells, Faculty of Engineering and Natural Sciences, Tampere University, P.O. Box 541, FI-33014 Tampere, Finland*

[ǂ]These authors contributed equally to this work

Abstract: Bismuth-based halide perovskite-inspired materials (PIMs) are gaining increasing attention as sustainable and stable alternatives to lead halide perovskites. However, many PIMs have wide band gaps (≥ 2 eV) and low electronic dimensionality, limiting their utility in optoelectronic applications. In this study, we introduce $Cs_2AgBi_2I_9$, a two-dimensional perovskite-inspired absorber achieved through partial substitution of Cs^+ with Ag^+ at the A-site of $Cs_3Bi_2I_9$. Single-crystal X-ray diffraction analysis reveals that silver atoms occupy edge sites in the hexagonal lattice, resulting in contracted lattice parameters compared to the parent $Cs_3Bi_2I_9$. The double A-cation substitution promotes orbital overlap between Ag-5s and I-6p orbitals, leading to a narrower band gap of 1.72 eV and a delocalized electronic structure in $Cs_2AgBi_2I_9$. Consequently, the 2D-PIM exhibits a three-order-of-magnitude lower electrical resistivity and an exceptional carrier mobility-lifetime product ($\mu\tau$) of 3.4 $\times 10^{-3}$ cm^2 V^{-1}, representing the highest among solution-processed Bi-based PIMs. Furthermore, low-temperature photoluminescence measurements indicate weak electron-phonon coupling, while transient absorption spectroscopy reveals extended hot-carrier lifetimes, suggesting efficient exciton transport in $Cs_2AgBi_2I_9$. Utilizing these exceptional charge transport properties, $Cs_2AgBi_2I_9$ photodetectors show remarkable broad spectral response. This work demonstrates the potential of a double A-site cation engineering strategy to develop low-toxicity PIMs with precisely tailored structural and optoelectronic properties.

1. Introduction

Bi(III)-based semiconductors are of particular interest among low-toxic perovskite-inspired materials (PIMs) due to the green elemental nature of bismuth, the ns^2 valence electronic configuration, the intrinsic environmental stability, and the high polarizability of Bi^{3+} can mitigate the defect formation probability in their band gap regime.[1,2] Despite these advantages, the optoelectronic performance of Bi-based devices typically falls short of their Pb-halide perovskite (LHP) counterparts, primarily because of the wider band gaps in Bi(III)

PIMs, which limits broadband light harvesting efficiency. For example, silver iodobismuthates with a band gap of ≈ 1.9 eV have only achieved around 5% efficiency in single-junction solar cells, significantly less than the 26% efficiency seen with LHP absorbers.[3,4] Similar limitations are observed with other Bi-based PIMs, which also feature wide band gaps,[5] like Cu_2AgBiI_6 (band gap of 2.0 eV) and Cs_2AgBiX_6 (band gap of 2.77 and 2.19 eV for compositions with X= Cl or Br, respectively). Another critical aspect is the electronic dimensionality of Bi-based PIMs, which typically is lower than that of LHPs. A lower dimensionality impedes efficient charge carrier transport, which is essential for achieving high device performance.[6] For instance, though the zero-dimensional (0D) $Cs_3Bi_2I_9$ is promising for various optoelectronic applications like electrochemical capacitors and scintillators[7–9] due to its high chemical and environmental stability, it possesses a structure consisting of face-sharing isolated metal iodide (Bi-I) octahedrons or clusters $[Bi_2I_9]^{3-}$. This results in a material with a wide band gap (~2 eV), high exciton binding energy (~300 meV), and a large charge carrier effective mass, which contrasts with the properties of conventional 3D LHPs.[10,11] The exciton dissociation into free carriers is challenging in 0D semiconductors at room temperature, which hinders their ability to reach optimal optoelectronic device performance closer to the Shockley-Queisser limit.[12] Moreover, the strong electron-phonon coupling typical of 0D semiconductors promotes charge carrier localization into self-trapped exciton (STE) states, further reducing their mobility and effective charge transport.[13–15]

Thus, to fully utilize the sustainability and stability advantages of Bi-based PIMs while maintaining a competitive efficiency in light-harvesting devices, it is essential to focus on materials with narrow band gaps and high structural and electronic dimensionality. One strategy to increase the structural dimensionality of $Cs_3Bi_2I_9$ involves modifying the A-site cations and X-site anions.[16,17] Such composition engineering strategy minimizes the strain in the crystal lattice, enabling corner sharing among the neighboring BiI_6 octahedrons and

transitioning them to a 2D-crystal structure.[17] For example, in 2D $Cs_3Bi_2I_6Br_3$, this corner-sharing octahedron leads to anisotropic optoelectronic properties.[18] However, this transition to a 2D structure does not necessarily increase the electronic dimensionality, as these 2D structures retain localized electronic bands akin to the original 0D structures. In other words, the electronic dimensionality of $Cs_3Bi_2I_9$ is not enhanced despite the increased structural dimensionality (from 0D to 2D).[19]

Another promising approach to enhance the structural dimensionality of 0D-$Cs_3Bi_2Br_9$ is introducing a monovalent Ag^+ cation at the B-site, as seen in the transformation to 3D-$Cs_2AgBiBr_6$ double perovskite. Where the interaction between the 4d orbital of Ag and the 4p orbital of Br modifies the band structure.[20] Within $Cs_2AgBiBr_6$, Ag and Bi are arranged alternatively at the octahedral sites (B-sites), allowing Ag to redistribute electronic charges across the atoms in alternating octahedra. This redistribution facilitates valence band hybridization, enhancing the separation of electron-hole pairs and thus improving carrier transport efficiency.[20] This highlights the importance of exploring Ag^+ cation substitution into 0D-$Cs_3Bi_2X_9$. However, incorporating Ag-cation in the B-site of 0D-$Cs_3Bi_2I_9$ is not feasible due to negative decomposition energy, which makes the formation of 3D-Cs_2AgBiI_6[21] thin films extremely challenging, with the only successful development of this material only at the nanoscale.[22] The synthetic challenges of 3D-Cs_2AgBiI_6 highlight the inherent instability of this material, as suggested by its tolerance factor of $0.63 << 1$.[23] This demonstrates the complex interplay between structural and electronic properties in enhancing the performance of Bi-based PIMs, emphasizing the urgent need of novel strategies required to optimize the optoelectronic properties of these materials.

So far, the introduction of Ag^+ cation at the A-site of 0D-$Cs_3Bi_2I_9$ has been limited to the complete replacement of the Cs cations with Ag, leading to a different class of PIMs, i.e., Ag iodobismuthates (Ag-Bi-I).[24] On the other hand, mixing A-site cations has enhanced the

structural and optoelectronic properties of other 0D PIMs.[25,26] These findings prompt further exploration into the effects of partial Ag^{+}-cation substitution at the A-site of 0D-$Cs_3Bi_2I_9$ on its structural, optical, and electronic properties. Additionally, finding the ideal cation stoichiometry in mixed cation-based PIMs poses a significant challenge, and this aspect is rarely explored with in-depth crystallographic insights in the existing literature. Therefore, a combination of crystallographic analysis and theoretical calculations holds the potential to open avenues for developing low-toxicity mixed cation-based PIMs for state-of-the-art device applications.

Herein, we employ a novel hot-spin coating method to synthesize 2D-$Cs_2AgBi_2I_9$ single crystals by in-situ Ag^{+}-cation incorporation in 0D-$Cs_3Bi_2I_9$. Single crystal X-ray diffraction (SC-XRD) verifies the partial substitution of Ag with Cs at the A-site, and the density functional theory (DFT) calculations describe the effect of the cation mixing at the A-site on the electronic band structures of 2D-$Cs_2AgBi_2I_9$. Interactions between Ag and I atoms in 2D-$Cs_2AgBi_2I_9$ result in dispersed electronic bands and a charge carrier mobility-lifetime product ($\mu\tau$) of 2.2×10^{-2} cm^2 V^{-1}, ensures the enhanced charge transport properties compared to the case of 0D-$Cs_3Bi_2I_9$. Finally, we demonstrate the remarkable photodetector performance of the 2D-$Cs_2AgBi_2I_9$ single-crystals over a broad spectral range and discuss how the improved electronic dimensionality of $Cs_2AgBi_2I_9$ is correlated with its excellent optoelectronic device performance.

2. Results and Discussion

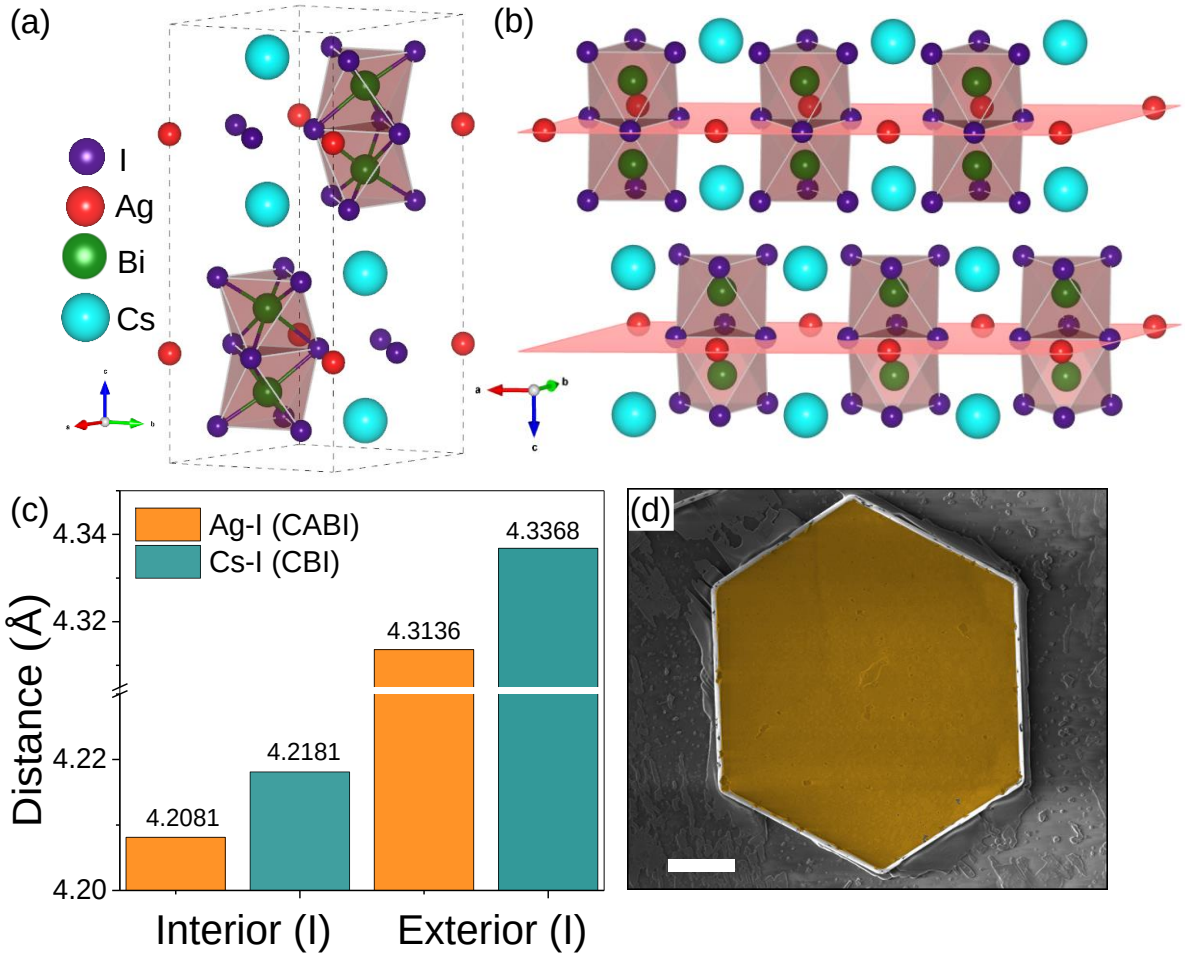

Figure 1: Crystallographic structural characterization of $Cs_2AgBi_2I_9$ using single crystal X-ray diffraction, (a) unit cell representation, (b) viewed along the c-axis. (c) Distance of iodine from A-site cation in $Cs_2AgBi_2I_9$ and $Cs_3Bi_2I_9$ crystals, (d) false colored SEM micrograph (scale bar, 10 µm) of $Cs_2AgBi_2I_9$ microcrystal.

We pioneer the partial substitution of Cs^+-cation with Ag^+ at the A-site of $Cs_3Bi_2I_9$, demonstrating the synthesis of a new 2D vacancy-ordered Bi-based PIM, namely $Cs_2AgBi_2I_9$. Our hypothesis posits that the introduction of smaller cations (Ag) facilitates the orbital overlap between I and Ag atoms, leading to the development of a layered structure along the (004) plane of $Cs_2AgBi_2I_9$, as illustrated in **Figure 1a** and **1b**. The synthesis of $Cs_2AgBi_2I_9$ utilizes a customized hot-spin casting method at 150°C (see **Figure S1**). Spin-coating of a stoichiometric precursor solution containing CsI, AgI, and BiI_3 in a 2:1:2 molar ratio onto a heated substrate triggers rapid solvent evaporation and super-saturation and initiates heterogeneous nucleation at the interface between the solution and substrate. The centrifugal force during the spinning

process removes excess solvent, thus promoting in-plane crystal growth. A subsequent vacuum drying for 12 hours facilitates the controlled growth of large, facet-oriented $Cs_2AgBi_2I_9$ microcrystals, ranging from 4–150 μm in size.

The hot-spin casting technique combines kinetic and spontaneous heat transfer with precise control of centrifugal force, enabling a simple and scalable method to synthesize facet-oriented $Cs_2AgBi_2I_9$ single crystals. $Cs_2AgBi_2I_9$ crystallizes in a hexagonal structure with the space group $P6_3/mmc$, having lattice parameters are a = 8.4137(12) Å, b = 8.4137 (12) Å, and c = 21.191(3) Å (see **Figure 1a, and Table S1**). This structure is similar to $Cs_3Bi_2I_9$ (see **Figure S2**), but Ag^+-cations substitute one-third of Cs^+-cations.[9] The Ag^+-cations are located at 2b Wyckoff position with (1, 0, ¾) fractional coordinates, while the Cs^+-cations remain at the 4f Wyckoff position (see **Figure 1a**). The Ag-I bond lengths for interior and exterior iodine atoms in $[Bi_2I_9]^{3-}$ clusters of 2D-$Cs_2AgBi_2I_9$ are shorter than the Cs-I bond lengths in $Cs_3Bi_2I_9$ (see **Figure 1c**), contributing to dispersed electronic bands. The Ag–I–Ag bond angle is found to be ~177.2°. High bond angles are known to endorse a superior orbital overlap, as observed in 3D halide perovskites. This enables a three-order-of-magnitude lower resistivity and significantly enhanced carrier transport in the 2D-$Cs_2AgBi_2I_9$ compared to 0D-$Cs_3Bi_2I_9$, as demonstrated in the following section. Furthermore, the Bi-I bond lengths in $Cs_2AgBi_2I_9$ with interior and exterior iodine atoms are decreased compared to $Cs_3Bi_2I_9$ (see **Table S6**). The incorporation of Ag^+ in $Cs_3Bi_2I_9$ shrinks the unit cell volume from 1314.7 to 1299.1 $Å^3$ and octahedral volume from 39.35 to 38.97 $Å^3$, supporting the observed decrease in Ag-I and Bi-I bond lengths. The reduction in lattice parameters in $Cs_2AgBi_2I_9$ is attributed to the smaller ionic radius of Ag^+ (128 pm) in comparison to Cs^+ (188 pm) in $Cs_3Bi_2I_9$ (see **Table S1-S6**).[27] Scanning electron microscopy (SEM) image, **Figure 1d**, illustrates the hexagonal $Cs_2AgBi_2I_9$ crystal with clearly defined edges. Overall, the structural and transmission electron microscopy (TEM) data confirm the successful partial substitution of Cs^+ with Ag^+ at the A-site of $Cs_3Bi_2I_9$,

in turn forming a new vacancy-ordered PIM, $Cs_2AgBi_2I_9$ (see **Figure S3, S4, and Note S1**). This transformation retains the hexagonal crystal structure but with adjusted unit cell parameters.

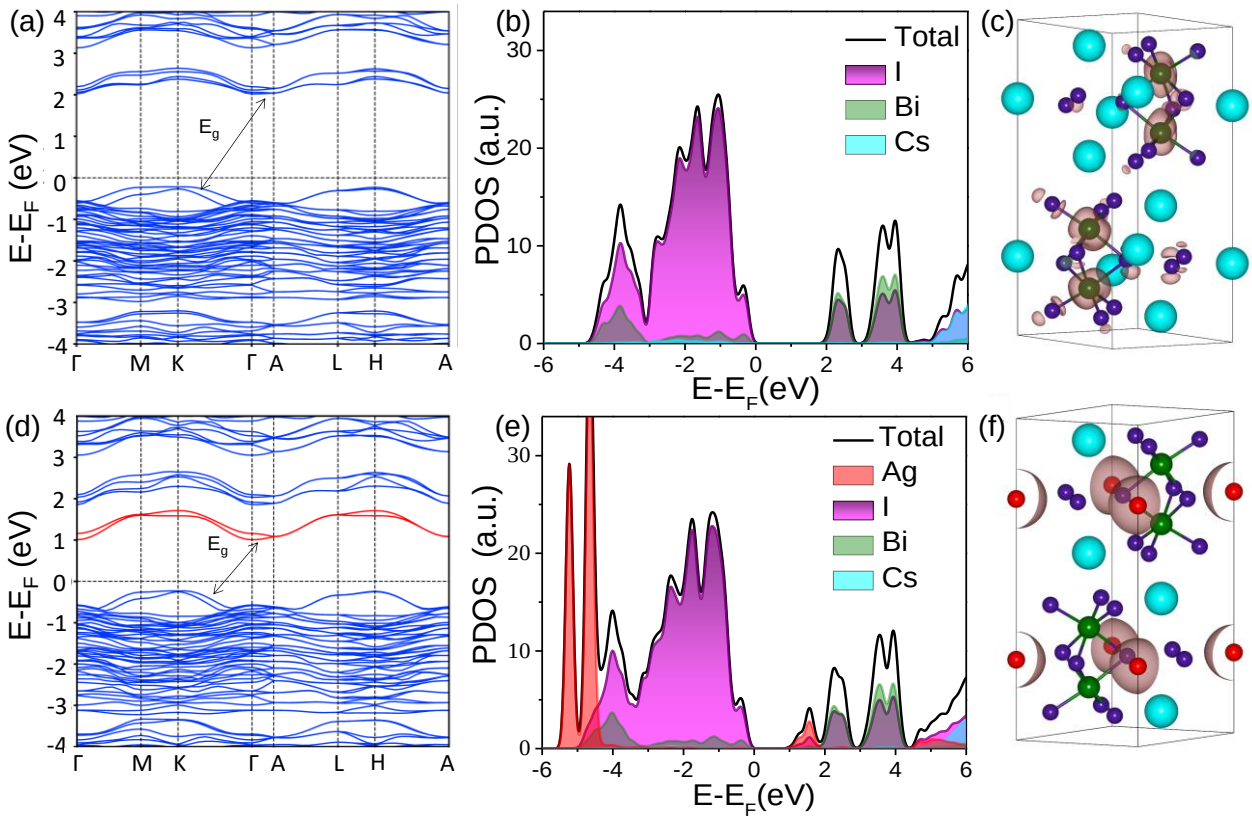

Figure 2. Calculated band structure (a, d), the projected density of states (b, e), and the charge density profiles (c, f) of $Cs_3Bi_2I_9$ and $Cs_2AgBi_2I_9$. The top (bottom) panels represent the results of $Cs_3Bi_2I_9$ ($Cs_2AgBi_2I_9$). The charge density plots are obtained with the conduction band minimum (by including the contribution from all k-points), and we used a 0.0006 e/Å^3 iso value in these plots.

To gain a theoretical understanding of the electronic band structure of $Cs_2AgBi_2I_9$, density functional theory (DFT) calculations were performed.[28,29] The approach involved optimizing the geometries of both $Cs_3Bi_2I_9$ and $Cs_2AgBi_2I_9$ using the Perdew-Burke-Ernzerhof (PBE) theory and then calculating their band structures and projected density of states (PDOS) using the HSE+SOC theory (see computational details).[30,31] The calculated indirect band gap for the $Cs_3Bi_2I_9$ is 2.27 eV (**Figure 2a)**, aligning with the reported literature values.[10,32,33] A noticeable reduction in the band gap (to 1.23 eV) was observed in $Cs_2AgBi_2I_9$, attributed to the formation of intermediate bands, a direct result of the Ag^+-cation substitution at the A-site, as

highlighted by red trace ~ 1 eV in **Figure 2d**. The PDOS plot of $Cs_2AgBi_2I_9$ (**Figure 2e**) suggests that these intermediate bands primarily originate from the Ag^+-cations, with minor

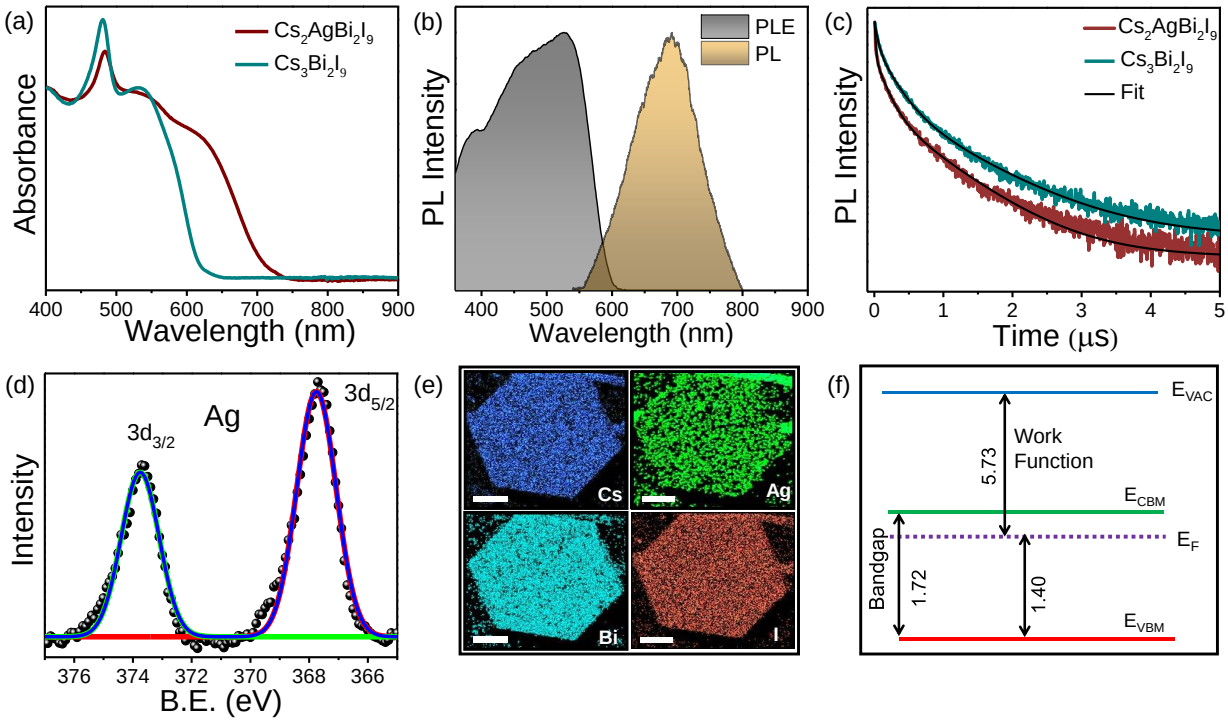

Figure 3: Optical and elemental characterization of $Cs_2AgBi_2I_9$ crystals. (a) UV-visible absorption spectra of $Cs_2AgBi_2I_9$ and $Cs_3Bi_2I_9$ crystals, (b) steady state PL spectrum (λ_{ex} = 532 nm) and corresponding PLE spectrum (λ_{em} = 692 nm) of $Cs_2AgBi_2I_9$ crystals, and (c) TRPL decay curves of $Cs_2AgBi_2I_9$ (λ_{em} = 690 nm) and $Cs_3Bi_2I_9$ (λ_{em} = 630 nm) crystals at room temperature with λ_{ex} = 360 nm. The thin lines on top of the data represent the exponential fits, (d) XPS core level spectra of Ag, (e) EDX elemental mapping of $Cs_2AgBi_2I_9$ crystals with constituent atoms, Cs, Ag, Bi, and I, scale bar, 100 microns (f) schematic illustration of the band positions while extracting Fermi level from UPS high binding energy region and band gap from Tauc plot.

contributions from I and Bi atoms, consistent with the decreased Ag-I bond length, **Figure 1c**. Further, **Figure S5** reveals that Ag-5s and I-6p orbitals mainly contribute to the conduction band, unlike the Ag d-orbital contributions observed in the valence band of $Cs_2AgBiBr_6$. The charge density plot in **Figure 2f** displays a spherical charge density near the Ag atoms, indicating the s-orbital character and validating the PDOS analysis.[20] Meanwhile, the conduction band in $Cs_3Bi_2I_9$ primarily arises due to the interactions between the Bi and I orbitals, see **Figure 2b**, which is also apparent from the charge density plot in **Figure 2c**.[34] To understand the origin of the reduced band gap in $Cs_2AgBi_2I_9$ compared to $Cs_3Bi_2I_9$, additional

simulations were performed to assess the effects of A-site cation substitution at different Wyckoff positions. Substituting Ag^+ with Cs^+ cations at 4f Wyckoff position (**Figure S6** and **Note S2**) revealed negligible impact on the band gap. These results confirm that the key to band gap decrease in $Cs_2AgBi_2I_9$ is the substitution at the 2b Wyckoff position (i.e., crystal structure, **Figure 1a**) manifesting orbital overlap between Ag (5s) and I (6p). Furthermore, the effective hole mass decreases with the partial substitution of Cs^+ with Ag^+, indicating improved orbital overlap and dispersive band structure. $Cs_2AgBi_2I_9$ demonstrates significantly lower effective masses for both electron and hole carriers in the in-plane (004) direction compared to the out-of-plane direction (see **Table S7**). This is attributed to the enhanced electronic dimensionality.

The absorption characteristics of $Cs_2AgBi_2I_9$ crystals, with an onset at 720 nm, demonstrate a redshift compared to $Cs_3Bi_2I_9$ crystals, which have an absorption onset at 620 nm, **Figure 3a**. The $Cs_2AgBi_2I_9$ crystals demonstrated a wide absorption compared to $Cs_3Bi_2I_9$ crystals. Also note that the intensity of the excitonic peak at 490 nm in 2D-$Cs_2AgBi_2I_9$ is weakened compared to that of the 0D-$Cs_3Bi_2I_9$, attributed to the decrease in the oscillator strength of excitonic absorption.[19] The estimated band gap of $Cs_2AgBi_2I_9$ is 1.72 eV (see the Tauc plot analysis (see **Figure S7, Note S3**), lower than the 1.99 eV band gap of $Cs_3Bi_2I_9$. A slight difference of 0.1 eV between the direct and indirect band gaps in $Cs_2AgBi_2I_9$ suggests it has a quasi-direct band gap nature. The variation in the band gap is consistent with DFT simulations; the overlap of Ag-5s and I-6p orbitals in $Cs_2AgBi_2I_9$ led to a decrease in the band gap (see **Figure 2d**). These orbital interactions between A-site cation and X-site anion are similar to the case of LHPs.[35–37]

The photoluminescence spectrum (PL) of $Cs_2AgBi_2I_9$ exhibits a peak at 695 nm, which is redshifted compared to the 630 nm peak of $Cs_3Bi_2I_9$ (see **Figure S8**). This shift aligns with the observed changes in absorption onset wavelengths (**Figure 3b**) and indicates the modified

band states due to the partial substitution of Ag^+-cation at the A-site, as supported by the crystallographic and DFT analyses. Confocal microscopy of $Cs_2AgBi_2I_9$ crystals discloses a consistent dark red emission, indicating crystal uniformity (see **Figure S9**), and it agrees with the steady-state PL emission. Time-resolved PL decay curves for both $Cs_2AgBi_2I_9$ and $Cs_3Bi_2I_9$ obtained at room temperature are presented in **Figure 3c** and show similar decay profiles, with average lifetimes of 540 and 650 ns, respectively (see **Table S8**). The slightly shorter PL lifetime in $Cs_2AgBi_2I_9$ compared to $Cs_3Bi_2I_9$ is ascribed to the increased dimensionality from 0D to 2D structures, following the incorporation of smaller cations at the A-site position, consistent with structures like $Cs_3Sb_2I_9$.[38] Therefore, the combination of broadband optical absorption and long carrier lifetimes (hundreds of nanoseconds) in $Cs_2AgBi_2I_9$ underscores its potential for application in broadband light-harvesting devices.

To identify the electronic structure and elemental composition of $Cs_2AgBi_2I_9$, X-ray photoelectron spectroscopy (XPS) and energy dispersive X-ray (EDX) mapping are performed. The XPS survey spectrum confirmed the presence of Cs, Ag, Bi, and I in $Cs_2AgBi_2I_9$ (**Figure S10** and **Table S9**). By examining the binding energies in the core-level spectra (see **Figures 3d, S11,** and **Table S9**), the oxidation states were evaluated: Cs and Ag were in +1 state, Bi was in +3, and I was in -1.[39–41] Note that, the +1 oxidation state of both Ag and Cs suggests a homovalent substitution at the A-site. This is in contrast with the Na^+ incorporation seen in $Cs_3Bi_2I_9$ at B-site.[42] EDX mapping, **Figure 3e**, demonstrated a uniform distribution of Cs, Ag, Bi, and I within the $Cs_2AgBi_2I_9$ crystal. The $Cs_2AgBi_2I_9$ crystals exhibit thermal stability up to 320°C, compared to $Cs_3Bi_2I_9$ (up to 442°C) and environmental stability up to one week (see **Figure S12** and **Note S4**); this can be attributed to the desorption of AgI.

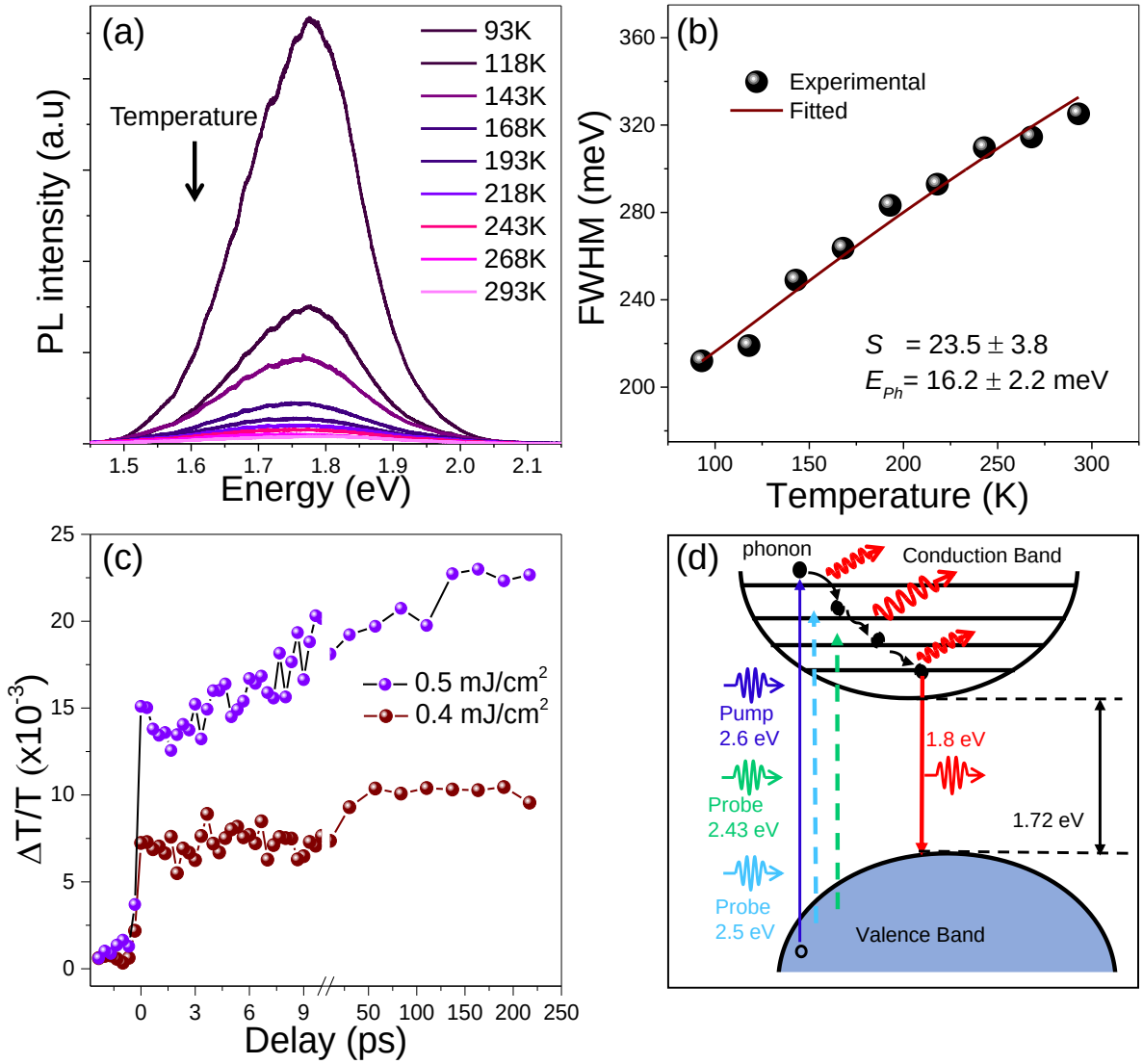

Figure 4. Temperature-dependent photoluminescence (PL) spectra of $Cs_2AgBi_2I_9$. (a) Evolution of PL spectra with respect to temperature and photon energy. (b) Progression of full-width half maxima (FWHM) as a function of temperature from 93 to 293 K. (c) Transient transmission changes of the 490 nm (2.5 eV) probe pulse at different temporal probe delays for $Cs_2AgBi_2I_9$ when excited at 470 nm (2.6 eV) with two excitation-pulse fluences, 0.4 and 0.5 mJ/cm^2 d) schematic depicting the relaxation pathways involved after photoexcitation in $Cs_2AgBi_2I_9$.

The work function of $Cs_2AgBi_2I_9$, estimated from the onset spectrum of ultraviolet photoelectron spectroscopy (UPS), is –5.73 eV (**Figure S13**). Analysis of the UPS tail spectrum discloses the difference between the Fermi level (E_F) and valance band maxima, i.e., E_F-E_{VBM} = 1.40 eV. A schematic illustrated in **Figure 3f** shows the electronic structure and energy band levels of $Cs_2AgBi_2I_9$. The E_F of $Cs_2AgBi_2I_9$ is closer to the conduction band minima (CBM), thus suggesting an n-type semiconductor nature. In comparison, $Cs_3Bi_2I_9$ exhibits p-type semiconductor characteristics (**Figure S14** and **Table S11**).[4344] Therefore, the

partial substitution of Cs^+ with Ag^+ in $Cs_3Bi_2I_9$ at the A-site leads to the formation of $Cs_2AgBi_2I_9$ with distinct electronic properties.

The temperature-dependent PL spectra of $Cs_2AgBi_2I_9$ were investigated in the range of 93-293 K, **Figure 4a**. The thermal quenching of photoluminescence intensity revealed an activation energy of 38 meV. This explains the low PL intensity observed at room temperature due to thermally assisted non-radiative recombination processes (see **Figure S15a and Note S5**).[6] As temperature decreases, $Cs_2AgBi_2I_9$ exhibited a narrowing of its PL peak. Steady-state PL spectra at different temperatures are deconvoluted into three Gaussian peaks, corresponding to direct, indirect, and self-trapped emission (STE) (see **Figure S15c-f** and **Note S6**). At lower temperatures, the decrease in non-radiative recombination, ascribed to restricted electron-phonon interaction, resulted in a predominance of direct transitions over indirect transitions and STE (**Figure S15b**).[45] Additionally, by fitting the PL intensity versus excitation power at room temperature, the power law exponent (k) for $Cs_2AgBi_2I_9$ and $Cs_3Bi_2I_9$ were extracted, as 0.70 and 0.47, respectively (**Figure S16c,f,** and **Note S7**).[13] The higher k value for $Cs_2AgBi_2I_9$, approaching the critical value of 1, indicates reduced non-radiative recombination and self-trapped emissions, which are crucial for optoelectronic devices. With increasing PL excitation intensity, $Cs_2AgBi_2I_9$ exhibited a blueshift in its PL peak, attributed to the carrier band filling effect due to the prolonged hot carrier lifetime discussed in the following section (see **Figure S16a,b,** and **Note S7**).[46,47] While $Cs_3Bi_2I_9$ displayed a redshifted PL peak due to strong electron-phonon coupling (see **Figure S16d,e**). Additionally, the minimal self-trapped emission in $Cs_2AgBi_2I_9$ at room temperature led to the examination of the Huang−Rhys electron-phonon coupling parameter (S), a measure of the average electron-phonon coupling strength that influences the number of phonons emitted during charge relaxation.[13] The corresponding phonon energy (E_{ph}) was calculated by fitting the temperature evolution of the

full width at half maximum (FWHM) of the PL emission peak (see **Figure 4b**) using the following equation 1.[13,48,49]

$$w(T) = 2.36\sqrt{S}E_{Ph}[\coth(\frac{E_{Ph}}{2k_BT})]^{\frac{1}{2}} \quad (1)$$

where w(T) represents the FWHM at temperature T, and k_B is the Boltzmann constant.[13,4849] The estimated S and E_{ph} are found to be 23.5 ± 3.8 and 16.2 ± 2.2 meV, respectively. Notably, the assessed E_{ph} of 16 meV (equivalent to 130.32 cm^{-1}) closely aligns with the strongest Raman band observed at 145.5 cm^{-1} (**Figure S17, Table S12,** and **Note S8**). The effective E_{Ph} is significantly higher than the 0D-$Cs_3Bi_2I_9$ (E_{ph} = 6 meV) and is on par with the 2D-$Rb_3Sb_2I_9$ (E_{ph} =20 meV) reported by Wessels et al.[13] The interaction with higher-energy phonon modes results in fewer correlated phonons during the relaxation process, leading to a lower S value compared to $Cs_3Bi_2I_9$ (S = 79.5 ± 3.8) and similar to the reported $Rb_3Sb_2I_9$ (21.2 ±1). This substantial reduction in the S parameter for 2D-$Cs_2AgBi_2I_9$ is likely due to the Ag-I interactions, which promote additional interactions within the Bi-I octahedron (with reduced degrees of freedom) to realize higher 2D electronic structure, as evidenced by DFT studies (see **Figures 2d** and **2f**).[13] Furthermore, the Longitudinal optical (LO) phonon energy (E_{LO}) is found to be 18 ±3 meV and corresponding LO phonon coupling parameter Υ_{LO} is 114 ± 7 meV. These values are significantly lower than those for other perovskites, such as $CsPb_2Br_5$(228 meV)[49], $Cs_2AgBiBr_6$ (226 meV),[50] and $Cs_3Bi_2I_6Cl_3$ (291.8 meV)[19], supporting low STE in $Cs_2AgBi_2I_9$.

Transient absorption measurements were performed to examine the carrier dynamics and electron-phonon interactions in $Cs_2AgBi_2I_9$, as detailed in **Figure S18**. The samples were excited at 470 nm (2.64 eV) pump and probing the carrier dynamics at 490 nm (2.53 eV) and 510 nm (2.43 eV). **Figure 4c** depicts transient transmission (ΔT/T) at two distinct pump fluences of 0.4 and 0.5 mJ/cm^2 using a 490 nm probe. The initial rapid change in probe pulse transmission, occurring within a few hundred femtoseconds, is attributed to photoinduced carriers falling to the indirect exciton band edge. Thus, a slight decrease in ΔT/T, measured in

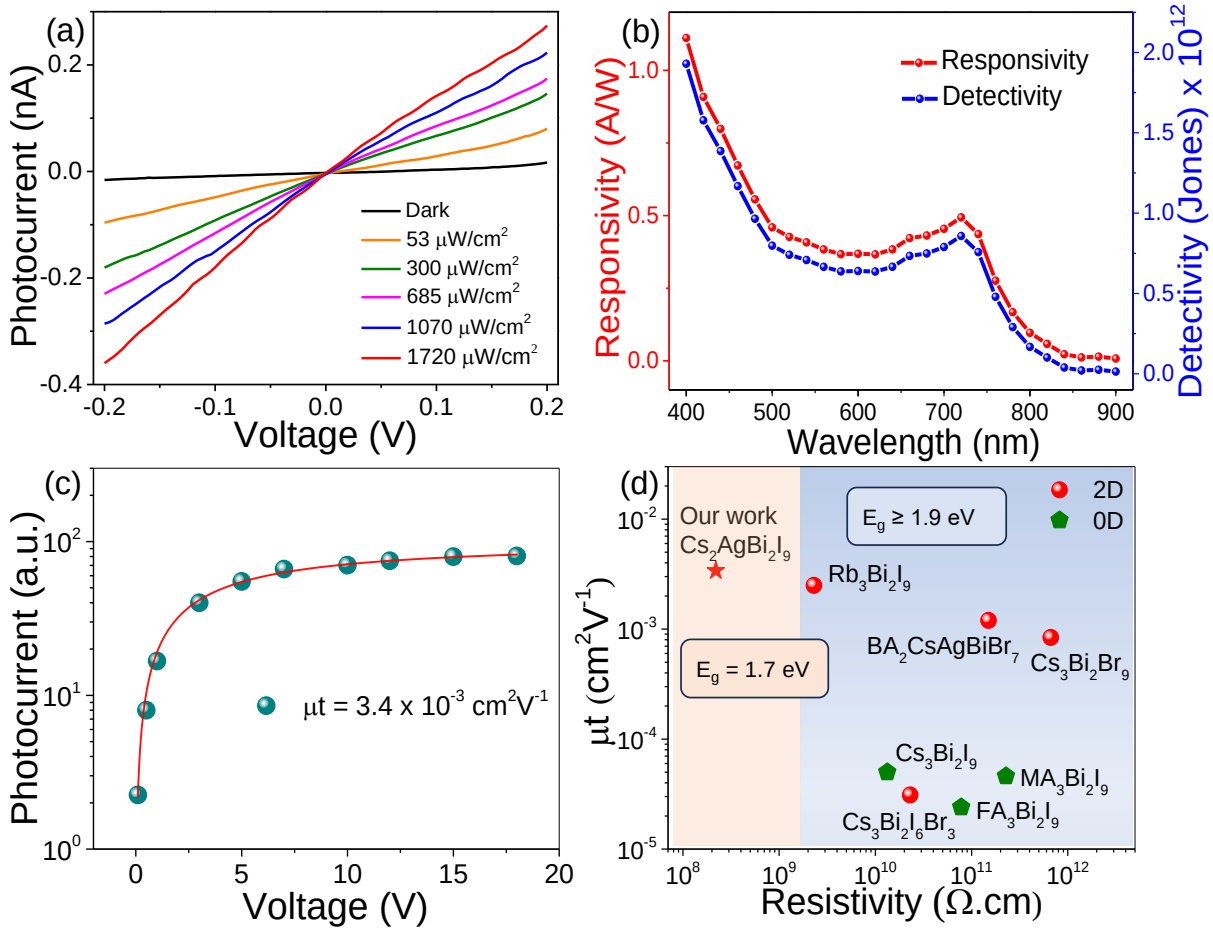

Figure 5: Photodetector performance of $Cs_2AgBi_2I_9$ crystal, (a) photocurrent as a function of voltage for different white light intensity from 53 to 1720 μW/ cm^2 and dark, (b) responsivity and detectivity as a function of wavelength at 0.2 V from 400 to 900 nm. (c) Carrier mobility and lifetime product ($\mu\tau$) estimation from photoconductivity measurements of $Cs_2AgBi_2I_9$ crystal, (d) comparison of μτ product as a function of resistivity with reported 0D and 2D Bi-based HPs.

a few picoseconds, is linked to carrier cooling. Afterward, ΔT/T rises with increasing pump-probe delay until 220 ps, ascribed to a weak electron-phonon scattering, causing a "phonon bottleneck" effect through Auger heating and subsequent lattice heating.[51,52] The estimated carrier density of ~ 10^{19} cm^{-3} at 470 nm excitation (see **Note S9**) aligns with these phonon bottleneck effects.[49] Enhancing the pump fluence to 0.5 mJ/cm² reveals more pronounced delayed carrier cooling, where weak electron-phonon scattering in $Cs_2AgBi_2I_9$ impedes the cooling of hot carriers, resulting in prolonged carrier cooling. Note that $Cs_3Bi_2I_9$ maintains a relatively stable ΔT/T due to strong electron-phonon scattering, leading to faster hot carrier cooling (**Figure S19**). Furthermore, $Cs_2AgBi_2I_9$ showed transmission changes for a wider

probe wavelength of 510 nm (2.5 eV) compared to $Cs_3Bi_2I_9$ (**Figure S20**), suggesting the presence of more electronic states, which is supported by DFT calculations. The processes following photoexcitation in $Cs_2AgBi_2I_9$ and $Cs_3Bi_2I_9$ are depicted in **Figure 4d** and **Figure S19b**, respectively.

The application of $Cs_2AgBi_2I_9$ crystals for optoelectronic devices is demonstrated through the construction of photodetectors using indium tin oxide (ITO) gap electrodes. A micro-crystal of $Cs_2AgBi_2I_9$ is positioned on the ITO electrodes via micro-imprint lithography (**Figure S21**).[53] The current-voltage (I-V) characteristics of the photodetector exhibit a gradual increase in photoresponse by raising the white light intensity (**Figure 5a**). The photosensitivity ($\Delta I/I_{dark}$) of the $Cs_2AgBi_2I_9$ photodetector, modulated by light intensity ranging from 53-1720 μW/cm², spans impressive photosensitivity from 379 to 1527%, thereby signifying high and reliable light-to-dark current conversion.[54] The linear dynamic range (LDR) shows a linear photoresponse within the light intensity range of 0.108 to 85 μW/cm², manifesting a remarkable LDR of 93 dB (**Figure S22**).[55] Spectral responsivity (R_λ) and detectivity, the fundamental figure of merits of a photodetector, were evaluated as a function of wavelength (**Figure 5b**).[5455] The photodetector exhibits R_λ encompassing the entire visible region (400–750 nm), with a peak value of 1.1 A/W at 400 nm. The detectivity follows a similar trend, peaking at 1.9×10^{12} Jones at 400 nm (see **Note S10**). The detectivity, R_λ, and external quantum efficiency (EQE) profiles aligned with the absorption of $Cs_2AgBi_2I_9$ crystals (**Figures 3a, 5b,** and **S23**). Unlike 0D-$Cs_3Bi_2I_9$-based photodetectors, which have a limited photoresponse in the narrow spectral range (300-600 nm),[4456] the $Cs_2AgBi_2I_9$ photodetector demonstrates photo-switching cycles under 670 nm modulated illumination (**Figure S24**), highlighting its broadband absorption capability. The device displays the best spectral response among Bi-based PIMs (as detailed in **Table S13**). The rise and fall times of the photodetector are 100 and 134 ms, respectively (see **Figure S25**). Overall, the $Cs_2AgBi_2I_9$ photodetector demonstrated reliable, robust, and

broadband photoresponse capabilities, setting a benchmark against other lead-free PIMs and being on par with Pb/Sn-based LHPs.[56,57] The dynamic photostability and repeatability[54,55] of the photodetector were thoroughly tested through more than 2462 on/off photo-switching cycles for 1 Hz input light pulses, illustrating its excellent stability and repeatability, **Figure S26.**

The photoresponse ability of $Cs_2AgBi_2I_9$ microcrystal is further assessed through photoconductivity measurement, and their carrier mobility-lifetime product ($\mu\tau$) is calculated using a modified Hecht equation (Eq. 2).[58–60]

$$J = \frac{J_0 \mu\tau V}{L^2} \frac{1-\exp\left(-\frac{L^2}{\mu\tau V}\right)}{1+\frac{LS}{\mu V}} - - - - - - - (2)$$

where J_0, μ, τ, V, and L represent the saturated current density, mobility, carrier lifetime, applied voltage, and the distance between two electrodes. This analysis revealed a significantly higher $\mu\tau$ product for 2D-$Cs_2AgBi_2I_9$ (3.4×10^{-3} cm² V⁻¹) along the plane (004), compared to 0D-$Cs_3Bi_2I_9$ (2.03×10^{-5} cm² V⁻¹) (see **Figure 5c)**.[61] The substantial improvement in μτ value for 2D-$Cs_2AgBi_2I_9$, along with its lower resistivity (2.2×10^8 Ω·cm) compared to other reported 0D and 2D Bi-halide PIMs (**Figure 5d**), highlights the enhanced charge transport of 2D-$Cs_2AgBi_2I_9$, attributed to the increased electronic dimensionality.[58,59,62–67] Additionally, the combination of a high μτ product and the effective atomic number (Z_{eff}) of 59.6 highlights the potential of $Cs_2AgBi_2I_9$ in next-generation radiation detectors.[68] Moreover, 2D-$Cs_2AgBi_2I_9$ exhibits a narrower band gap within Bi-based halide perovskites. The combination of enhanced charge transport and tunable band gap makes 2D-$Cs_2AgBi_2I_9$ a promising candidate for various optoelectronic applications.

3. Conclusion

We herein present the synthesis of a novel Bi-based PIM, 2D-$Cs_2AgBi_2I_9$ single crystal, using a hot-spin casting technique, leveraging the in-situ partial substitution of Ag^+-cation into the A-site of 0D-$Cs_3Bi_2I_9$. The crystal structure of as-obtained crystals was successfully

confirmed using SC-XRD analysis. Detailed crystal structural analysis and DFT simulations indicate that substituting Ag^{+}-cations at $1/3^{rd}$ of the A-sites leads to a reduced lattice parameter and enables the interactions between Ag-5s and I-6p orbitals, introducing additional band states near the conduction band. This results in a narrower band gap of 1.72 ev for 2D-$Cs_2AgBi_2I_9$, which is 0.27 eV smaller than that of 0D-$Cs_3Bi_2I_9$. These structural and electronic modifications in $Cs_2AgBi_2I_9$ lead to weak electron-phonon coupling and a "phonon bottleneck" effect, successfully extending the lifetimes of hot carriers. As a result, 2D-$Cs_2AgBi_2I_9$ exhibits significantly lower resistivity (2.2×10^8 Ω·cm) and improved charge carrier transport, confirmed by a higher $\mu\tau$ product of 3.4×10^{-3} cm^2 V^{-1}.

Furthermore, a photodetector based on the 2D-$Cs_2AgBi_2I_9$ single crystal demonstrates a broad spectral response, with a high responsivity of 1.1 A/W and a remarkable detectivity of 10^{12} Jones. These advanced optoelectronic characteristics highlight the potential of double A-site cation engineering in developing efficient Bi-based PIMs and suggest a shift from the traditional 3:2:9 stoichiometry to a more versatile 2:1:2:9 composition like $Cs_2AgBi_2I_9$. Our findings offer new avenues for designing next-generation light absorbers with a broad spectral response for diverse optoelectronic applications.

4. Experimental Methods

Materials: CsI, AgI, and BiI_3 precursor materials were purchased from Sigma Aldrich. DMSO and IPA solvent chemicals were bought from Merck. PDMS and corresponding curing agent were procured from Dow (The Dow Chemical Company). All the chemicals were used without further purification.

Synthesis of $Cs_2AgBi_2I_9$ and $Cs_3Bi_2I_9$ crystals: The precursor solution for the synthesis of $Cs_2AgBi_2I_9$ crystals is prepared by mixing CsI, AgI, and BiI_3 at a stoichiometric ratio of (2:1:1) in 4 ml DMSO followed by magnetically stirring (800 rpm) in a closed vial overnight at a constant temperature of 70 ^{o}C. After overnight stirring, the clear precursor solution with 0.5

mg/ml concentration is cooled to room temperature and spin-coated on the desired substrate. The glass substrates were cleaned in soap water, milli-Q water, acetone, and IPA by performing ultrasonication in each solution for 10 minutes. Further, the glass substrates were cleaned using the UV-Ozone cleaner for 1 hour. The cleaned glass substrates are heated at 150 ^{o}C for 8 minutes and instantaneously spin-coated (Apex Instruments: SpinNXGP1) with the precursor solution. $Cs_2AgBi_2I_9$ crystals were synthesized following a two-step spin-coating configuration, where spinning is performed at 200 rpm for 20 s and 1000 rpm for 60 s. Finally, the glass substrates were kept in a vacuum desiccator overnight for complete evaporation of the solvent. Subsequently, the precursor solution for $Cs_3Bi_2I_9$ crystals is prepared by stoichiometrically adding CsI and BiI_3 in a 3:2 ratio in 4 ml DMSO. A similar synthesis methodology is adopted for the fabrication of $Cs_3Bi_2I_9$ crystals.

Characterization of $Cs_2AgBi_2I_9$ crystals: X-ray diffraction (XRD) measurements of $Cs_2AgBi_2I_9$ crystals were carried out in Bruker AXS D8 Advanced equipment (40 kV, 40 mA, wavelength ~ 0.15406 nm) with Cu Kα radiation. The single crystal XRD data were recorded at room temperature through irradiation of Mo Kα (λ = 0.7107 Å) from Bruker D8 VENTURE with 1μS 3.0 microfocus X-ray source. Diffracted data was collected through a CMOS detector equipped with Bruker D8 VENTURE using the software package APEX III. The collected data were reduced and refined using ShelXL in Olex2. The solved crystal structure was visualized using Vesta. Scanning electron microscopy (SEM) and Energy Dispersive X-ray analysis (EDX) of $Cs_2AgBi_2I_9$ crystals were obtained through FESEM (JEOL JSM-7500F). SAED patterns of Cs2AgBi2I9 crystals were collected from an ultrahigh-resolution field emission gun transmission electron microscope (JEOL, JEM 2100 F). The UV-vis spectra (α/s) of crystals were measured in reflectance mode using a Jasco V-750 Spectrometer. The reflection data was converted to absorbance using the Kubelka-Munk equation.[69-70] Raman and PL spectra of films were acquired using Lab RAM-HR Horiba France with a 532 nm laser as an excitation source.

Temperature-dependent PL measurements were recorded by placing the sample into the Linkam stage (THMS600), which was integrated with the LabRAM-HR Raman microscope. The acquisition time used for acquiring Raman spectra was 25 seconds, while it was 5 seconds for recording PL spectra. TCSPC measurements are carried out in the Horiba Scientific Deltaflex Modular Fluorescence Lifetime System excited with a 360 nm LED source. Zeiss LSM, 800 with a GaAsP PMT detector, is utilized for confocal microscopy with an excitation wavelength of 561 nm. X-ray photoelectron spectroscopy (XPS) core level and valance band data were collected using an Omicron (series 0571) system with micro-focused (100 µm, 25 W, 15 kV) monochromatic Al Kα source (hν = 1486.6 eV), a hemispherical analyzer and a multichannel detector. Ultraviolet photoelectron Spectroscopy (UPS) measurements were carried out using PHI 5000 Versa Probe III with 21.2 eV photon energy. Thermogravimetric analysis (TGA) data is recorded with TGA 4000 PerkinElmer. Raman spectra of films were acquired using LabRAM-HR Horiba France with a 532 nm laser as an excitation source. To perform the pump-probe transmission, we utilize the output of two optical parametric amplifier lasers (OPA), as shown in **Figure (S18)**. This is dual-color pump-probe geometry, where the pump part of OPA is kept at 470 nm while the probe beam is at 490 nm and 510 nm for two different measurements. The Amplifier laser is from Coherent, USA, and the OPA femtosecond laser system is from Light Conversion. The Amplifier system operates at 1 KHz, 35 fs at 800 nm. The OPA's are tuneable from 200 nm to 2000 nm. The pulse width in our measurement is 70 fs. The time-resolved pump-probe transmission measurement is performed at room temperature.

Computational Details: All electronic structure calculations were performed using the density functional theory (DFT) within the framework of the projected augmented-wave method (PAW),[29], as implemented in the Vienna Ab initio Simulation Package (VASP).[29] For all the elements, we considered the standard valence configurations: Cesium: $5s^2 5p^6 6s^1$, Bismuth:

$5d^{10}6s^26p^3$, Iodine: $5s^25p^5$, Silver: $4d^{10}5s^1$. All the geometry optimization calculations were performed using the PBE functional[30] with a 400 eV plane-wave cutoff and with a 5✕5✕2 Monkhorst-Pack[31] k-mesh to sample the Brillouin zone. The energy and force convergence criteria were set at 10^{-5} eV and 0.01 eV/Å, respectively. We computed the band structure and density of states (DOS) at two levels of theory. At the Perdew–Burke-Ernzerhof (PBE) level of theory, we used a 15×15×6 k-mesh for DOS, and for band structure, 20 k-points were considered between each set of high-symmetry k-points. Additionally, since PBE functional is known to underestimate the band gap of halide perovskite materials,[3132] we computed the DOS and band structure (with the geometries obtained at the PBE level of theory) using the screened hybrid exchange-correlation functional, HSE06.[34] Also, we incorporated the spin-orbit coupling (SOC) corrections in these calculations. For calculating the band structure at the HSE06+SOC level of theory, ten k-points were considered between the high-symmetry points, and the same k-mesh (total 71 k-points) was used to obtain the DOS. Unless stated explicitly, all the DOS and band structure results presented in this work are obtained with the HSE06 functional along with the SOC corrections. All the relevant post-processing data were obtained using the VASPKIT program [71] and plotted using the in-house Python scripts. VESTA was used to visualize the optimized structures and generate the charge-density plots. The effective masses of electrons and holes are calculated using the equation $m^* = \hbar^2/(\partial^2E/\partial k^2)$, where the values of $\partial^2E/\partial k^2$ are estimated from the bandstructure plots using the least squares fit technique, as implemented in the *effmass* software package.[72]

Fabrication of $Cs_2AgBi_2I_9$ crystal-based photodetector: The $Cs_2AgBi_2I_9$ crystal-derived photodetector is fabricated using an ITO (24 µm) and Au (30 µm) gap electrode in in-plane geometry. The micro-imprint lithography transfer technique is employed to transfer the crystals from the grown glass substrate to the patterned ITO gap electrodes. First, a few drops of IPA were sprinkled over the grown substrate to detach crystals from the glass surface. A rectangular

PDMS block is utilized to transfer the crystals to the desired substrate. After the transfer of crystals, the device is heated at 100 ℃ for 15 minutes to remove the residual IPA. The active area of the $Cs_2AgBi_2I_9$ crystals-derived photodetector is. 6.68×10^{-9} m^2. Photoconductivity measurements for carrier mobility and lifetime ($\mu\tau$) product estimation are carried out using an in-planer device structure (Au/MoO_3/$Cs_2AgBi_2I_9$/MoO_3/Au). A thermal evaporation system (Hind High Vacuum - 12A4D, India) is used to deposit 20 nm of MoO_3 and 50 nm of Au electrodes on $Cs_2AgBi_2I_9$ crystals. The photocurrent measurements are performed using the Keithley 2634B system in two-terminal configurations. The wavelength-dependent photocurrent measurements are performed using the Holmarc high throughput F4 spectral illumination system. The white light intensity is modulated using commercially available white LED light and controlled using a mobile application.

[CCDC 2225174 contains the supplementary crystallographic data for this paper. These data can be obtained free of charge from the Cambridge Crystallographic Data Centre via www.ccdc.cam.ac.uk/data_request/cif.]

ASSOCIATED CONTENT

Supporting Information: The Supporting Information is available free of charge at [URL]. It includes a schematic of experimental methods, crystallographic tables of $Cs_2AgBi_2I_9$ and $Cs_3Bi_2I_9$, powder XRD and TEM data, additional theoretical calculations of PDOS and effective mass for $Cs_2AgBi_2I_9$ and $Cs_3Bi_2I_9$, XPS and UPS data, XRD evolution with time, TGA data with analysis, additional experimental data analysis estimated from low-temperature PL and pump-probe measurements with explanations, Raman spectra comparison, and photodetector figure-of-merit calculations and literature comparison.

The authors have cited additional references within the Supporting Information.

AUTHOR INFORMATION

Corresponding Author

* E-mail: mallik2arjun@gmail.com, saiskdmrao@iacs.res.in

[ǂ]These authors contributed equally to this work

Author contributions

M.H. and K.S. conducted experiments, performed analysis, and conceived this work. M.S.S. and K.V. contributed through additional experiments and analysis. A.N., S.K.R., and S.S.R.K.C.Y carried out theoretical simulations and analysis. S.K., A.S., S.K., and P.K.V. conducted the pump-probe measurements and analysis. M.C. G.K.G. and P.V. contributed to the analysis and interpretation. K. D. M. R. was the project designer and supervisor, overseeing the overall progress. All authors contributed to the writing of the manuscript.

Notes

The authors declare no conflict of interest.

Acknowledgments

M.H. and M.S.S. acknowledge UGC for fellowship and IACS for research facilities. A.N. acknowledges the Ministry of Education for the PMRF fellowship (Project No: SB22230898CYPMRF008973). K.S. acknowledges CSIR for fellowship. K.D.M.R. and P.K.V. acknowledge the Science and Engineering Research Board (SERB) projects CRG/2022/004873 & SRG/2022/000118 and UGC-DAE CRS/2022-23/01/676 projects for financial support. S.K.R. acknowledges the National Supercomputing Mission (NSM) for providing computing resources of ‘PARAM Shakti’ at IIT Kharagpur, which is implemented by C-DAC and supported by the Ministry of Electronics and Information Technology (MeitY) and Department of Science and Technology (DST), Government of India. S.S.R.K.C.Y. acknowledges the financial support of IIT Madras through the MPHASIS faculty fellowship and its new faculty support grants NFSG (IP2021/0972CY/NFSC008973), NFIG (RF2021/0577CY/NFIG008973), and DST-SERB (SRG/2021/001455). P.V. acknowledges the Research Council of Finland, Decision No. 347772. G.K.G. acknowledges Tampere Institute for Advanced Study for the postdoctoral funding. This work was part of the Research Council of Finland Flagship Programme, Photonics Research and Innovation (PREIN), Decision No. 320165. The authors acknowledge Madhubrata Ghora and Prabhat Majumdar for

supporting single crystal measurements. KV acknowledges the Central Sophisticated Instrumentation Facility (CSIF), BITS Pilani, K K Birla Goa campus for the Raman facility.

References

(1) Mohan, R. Green Bismuth. *Nat. Chem.* **2010**, *2* (4), 336–336.

(2) Brandt, R. E.; Stevanović, V.; Ginley, D. S.; Buonassisi, T. Identifying Defect-Tolerant Semiconductors with High Minority-Carrier Lifetimes: Beyond Hybrid Lead Halide Perovskites. *MRS Commun.* **2015**, *5* (2), 265–275.

(3) Pai, N.; Lu, J.; Gengenbach, T. R.; Seeber, A.; Chesman, A. S. R.; Jiang, L.; Senevirathna, D. C.; Andrews, P. C.; Bach, U.; Cheng, Y. B.; Simonov, A. N. Silver Bismuth Sulfoiodide Solar Cells: Tuning Optoelectronic Properties by Sulfide Modification for Enhanced Photovoltaic Performance. *Adv. Energy Mater.* **2019**, *9* (5), 1–11.

(4) NREL. Best Research-Cell Efficiencies. https://www.nrel.gov/pv/cell-efficiency.html (accessed July 25, 2024).

(5) Sansom, H. C.; Longo, G.; Wright, A. D.; Buizza, L. R. V; Mahesh, S.; Wenger, B.; Zanella, M.; Abdi-Jalebi, M.; Pitcher, M. J.; Dyer, M. S.; Manning, T. D.; Friend, R. H.; Herz, L. M.; Snaith, H. J.; Claridge, J. B.; Rosseinsky, M. J. Highly Absorbing Lead-Free Semiconductor Cu 2 AgBiI 6 for Photovoltaic Applications from the Quaternary CuI–AgI–BiI 3 Phase Space. *J. Am. Chem. Soc.* **2021**, *143* (10), 3983–3992.

(6) Jagt, R. A.; Bravić, I.; Eyre, L.; Gałkowski, K.; Borowiec, J.; Dudipala, K. R.; Baranowski, M.; Dyksik, M.; van de Goor, T. W. J.; Kreouzis, T.; Xiao, M.; Bevan, A.; Płochocka, P.; Stranks, S. D.; Deschler, F.; Monserrat, B.; MacManus-Driscoll, J. L.; Hoye, R. L. Z. Layered BiOI Single Crystals Capable of Detecting Low Dose Rates of X-Rays. *Nat. Commun.* **2023**, *14* (1), 2452.

(7) Shin, J.; Kim, M.; Jung, S.; Kim, C. S.; Park, J.; Song, A.; Chung, K. B.; Jin, S. H.; Lee, J. H.; Song, M. Enhanced Efficiency in Lead-Free Bismuth Iodide with Post Treatment Based on a Hole-Conductor-Free Perovskite Solar Cell. *Nano Res.* **2018**, *11* (12), 6283–6293.

(8) Adams, K.; Mallows, J.; Li, T.; Kampouris, D.; Thijssen, J. H. J.; Robertson, N. Cs3Bi2I9 as High-Performance Electrode Material Achieving High Capacitance and Stability in an Economical Supercapacitor. *J. Phys. Energy* **2019**, *1* (3), 34001.

(9) Zhang, Y.; Liu, Y.; Xu, Z.; Ye, H.; Yang, Z.; You, J.; Liu, M.; He, Y.; Kanatzidis, M. G.; Liu, S. (Frank). Nucleation-Controlled Growth of Superior Lead-Free Perovskite Cs3Bi2I9 Single-Crystals for High-Performance X-Ray Detection. *Nat. Commun.* **2020**, *11* (1), 1–11.

(10) Qi, Z.; Fu, X.; Yang, T.; Li, D.; Fan, P.; Li, H.; Jiang, F.; Li, L.; Luo, Z.; Zhuang, X.; Pan, A. Highly Stable Lead-Free Cs3Bi2I9 Perovskite Nanoplates for Photodetection Applications. *Nano Res.* **2019**, *12* (8), 1894–1899.

(11) Zhang, L.; Liu, C.; Wang, L.; Liu, C.; Wang, K.; Zou, B. Pressure-Induced Emission Enhancement, Band-Gap Narrowing, and Metallization of Halide Perovskite Cs 3 Bi 2 I 9. *Angew. Chemie Int. Ed.* **2018**, *57* (35), 11213–11217.

(12) Rieger, S.; Bohn, B. J.; Döblinger, M.; Richter, A. F.; Tong, Y.; Wang, K.; Müller-Buschbaum, P.; Polavarapu, L.; Leppert, L.; Stolarczyk, J. K.; Feldmann, J. Excitons and Narrow Bands Determine the Optical Properties of Cesium Bismuth Halides. *Phys. Rev. B* **2019**, *100* (20), 201404.

(13) McCall, K. M.; Stoumpos, C. C.; Kostina, S. S.; Kanatzidis, M. G.; Wessels, B. W. Strong Electron–Phonon Coupling and Self-Trapped Excitons in the Defect Halide Perovskites A3M2I9 (A = Cs, Rb; M = Bi, Sb). *Chem. Mater.* **2017**, *29* (9), 4129–4145.

(14) He, X.; Tailor, N. K.; Satapathi, S.; Brgoch, J.; Yang, D.-S. Strong Coupling of Self-Trapped Excitons to Acoustic Phonons in Bismuth Perovskite Cs3Bi2I9. *Adv. Opt. Mater.* **2023**, *n/a* (n/a), 2300199.

(15) Rondiya, S. R.; Jagt, R. A.; MacManus-Driscoll, J. L.; Walsh, A.; Hoye, R. L. Z. Self-Trapping in Bismuth-Based Semiconductors: Opportunities and Challenges from Optoelectronic Devices to Quantum Technologies. *Appl. Phys. Lett.* **2021**, *119* (22).

(16) Nie, R.; Sumukam, R. R.; Reddy, S. H.; Banavoth, M.; Seok, S. Il. Lead-Free Perovskite Solar Cells Enabled by Hetero-Valent Substitutes. *Energy Environ. Sci.* **2020**, *13* (8), 2363–2385.

(17) Hodgkins, T. L.; Savory, C. N.; Bass, K. K.; Seckman, B. L.; Scanlon, D. O.; Djurovich, P. I.; Thompson, M. E.; Melot, B. C. Anionic Order and Band Gap Engineering in Vacancy Ordered Triple Perovskites. *Chem. Commun. (Camb).* **2019**, *55* (21), 3164–3167.

(18) Sun, Q.; Xiao, B.; Ji, L.; Zhao, D.; Liu, J.; Zhang, W.; Zhu, M.; Jie, W.; Zhang, B.-B.; Xu, Y. Effect of Dimensional Expansion on Carrier Transport Behaviors of the Hexagonal Bi-Based Perovskite Crystals. *J. Energy Chem.* **2022**, *66*, 459–465.

(19) McCall, K. M.; Stoumpos, C. C.; Kontsevoi, O. Y.; Alexander, G. C. B.; Wessels, B. W.; Kanatzidis, M. G. From 0D-Cs3Bi2I9 to 2D-Cs3Bi2I6Cl3 : Dimensional Expansion Induces a Direct Band Gap but Enhances Electron-Phonon Coupling. *Chem. Mater.* **2019**, *31* (7), 2644–2650.

(20) Shi, M.; Li, G.; Tian, W.; Jin, S.; Tao, X.; Jiang, Y.; Pidko, E. A.; Li, R.; Li, C. Understanding the Effect of Crystalline Structural Transformation for Lead-Free Inorganic Halide Perovskites. *Adv. Mater.* **2020**, *32* (31), 1–8.

(21) Savory, C. N.; Walsh, A.; Scanlon, D. O. Can Pb-Free Halide Double Perovskites Support High-Efficiency Solar Cells? *ACS Energy Lett.* **2016**, *1* (5), 949–955.

(22) Liu, Y.; Huang, Y.; Yang, Z.; Li, Y.; Xu, J.; Li, H.; Chen, W.; Chen, K. Hexagonal Lead-Free Cs 2 AgBiI 6 Perovskite Nanocrystals: A Promising Material for Solar Cell Application. *ACS Appl. Energy Mater.* **2023**, *6* (10), 5188–5196.

(23) Vishnoi, P.; Seshadri, R.; Cheetham, A. K. Why Are Double Perovskite Iodides so Rare? *J. Phys. Chem. C* **2021**, *125* (21), 11756–11764.

(24) Kulkarni, A.; Ünlü, F.; Pant, N.; Kaur, J.; Bohr, C.; Jena, A. K.; Öz, S.; Yanagida, M.; Shirai, Y.; Ikegami, M.; Miyano, K.; Tachibana, Y.; Chakraborty, S.; Mathur, S.; Miyasaka, T. Concerted Ion Migration and Diffusion-Induced Degradation in Lead-Free Ag 3 BiI 6 Rudorffite Solar Cells under Ambient Conditions. *Sol. RRL* **2021**, *5* (8), 1–10.

(25) Choi, Y. K.; Heo, J. H.; Hong, K.-H.; Im, S. H. Dual-Site Mixed Layer-Structured FA x

Cs 3−x Sb 2 I 6 Cl 3 Pb-Free Metal Halide Perovskite Solar Cells. *RSC Adv.* **2020**, *10* (30), 17724–17730.

(26) Lamminen, N.; Grandhi, G. K.; Fasulo, F.; Hiltunen, A.; Pasanen, H.; Liu, M.; Al-Anesi, B.; Efimov, A.; Ali-Löytty, H.; Lahtonen, K.; Mäkinen, P.; Matuhina, A.; Muñoz-García, A. B.; Pavone, M.; Vivo, P. Triple A-Site Cation Mixing in 2D Perovskite-Inspired Antimony Halide Absorbers for Efficient Indoor Photovoltaics. *Adv. Energy Mater.* **2023**, *13* (4).

(27) Shannon, R. D. Revised Effective Ionic Radii and Systematic Studies of Interatomic Distances in Halides and Chalcogenides. *Acta Crystallogr. Sect. A* **1976**, *32* (5), 751–767.

(28) Blöchl, P. E. Projector Augmented-Wave Method. *Phys. Rev. B* **1994**, *50* (24), 17953–17979.

(29) Kresse, G.; Furthmüller, J. Efficient Iterative Schemes for Ab Initio Total-Energy Calculations Using a Plane-Wave Basis Set. *Phys. Rev. B* **1996**, *54* (16), 11169–11186.

(30) Ernzerhof, M.; Scuseria, G. E. Assessment of the Perdew–Burke–Ernzerhof Exchange-Correlation Functional. *J. Chem. Phys.* **1999**, *110* (11), 5029–5036.

(31) Pack, J. D.; Monkhorst, H. J. "Special Points for Brillouin-Zone Integrations"—a Reply. *Phys. Rev. B* **1977**, *16* (4), 1748–1749.

(32) Mosconi, E.; Amat, A.; Nazeeruddin, M. K.; Grätzel, M.; De Angelis, F. First-Principles Modeling of Mixed Halide Organometal Perovskites for Photovoltaic Applications. *J. Phys. Chem. C* **2013**, *117* (27), 13902–13913.

(33) Wiktor, J.; Rothlisberger, U.; Pasquarello, A. Predictive Determination of Band Gaps of Inorganic Halide Perovskites. *J. Phys. Chem. Lett.* **2017**, *8* (22), 5507–5512.

(34) Heyd, J.; Scuseria, G. E.; Ernzerhof, M. Hybrid Functionals Based on a Screened Coulomb Potential. *J. Chem. Phys.* **2003**, *118* (18), 8207–8215.

(35) Byranvand, M. M.; Otero-Martínez, C.; Ye, J.; Zuo, W.; Manna, L.; Saliba, M.; Hoye, R. L. Z.; Polavarapu, L. Recent Progress in Mixed A-Site Cation Halide Perovskite Thin-Films and Nanocrystals for Solar Cells and Light-Emitting Diodes. *Adv. Opt. Mater.* **2022**, *10* (14), 2200423.

(36) Gao, W.; Chen, C.; Ran, C.; Zheng, H.; Dong, H.; Xia, Y.; Chen, Y.; Huang, W. A-Site Cation Engineering of Metal Halide Perovskites: Version 3.0 of Efficient Tin-Based Lead-Free Perovskite Solar Cells. *Adv. Funct. Mater.* **2020**, *30* (34), 2000794.

(37) Hazarika, A.; Zhao, Q.; Gaulding, E. A.; Christians, J. A.; Dou, B.; Marshall, A. R.; Moot, T.; Berry, J. J.; Johnson, J. C.; Luther, J. M. Perovskite Quantum Dot Photovoltaic Materials beyond the Reach of Thin Films: Full-Range Tuning of A-Site Cation Composition. *ACS Nano* **2018**, *12* (10), 10327–10337.

(38) Correa-Baena, J. P.; Nienhaus, L.; Kurchin, R. C.; Shin, S. S.; Wieghold, S.; Putri Hartono, N. T.; Layurova, M.; Klein, N. D.; Poindexter, J. R.; Polizzotti, A.; Sun, S.; Bawendi, M. G.; Buonassisi, T. A-Site Cation in Inorganic A3Sb2I9 Perovskite Influences Structural Dimensionality, Exciton Binding Energy, and Solar Cell Performance. *Chem. Mater.* **2018**, *30* (11), 3734–3742.

(39) Igbari, F.; Wang, R.; Wang, Z.-K.; Ma, X.-J.; Wang, Q.; Wang, K.-L.; Zhang, Y.; Liao,

L.-S.; Yang, Y. Composition Stoichiometry of Cs2AgBiBr6 Films for Highly Efficient Lead-Free Perovskite Solar Cells. *Nano Lett.* **2019**, *19* (3), 2066–2073.

(40) Kato, Y.; Ono, L. K.; Lee, M. V.; Wang, S.; Raga, S. R.; Qi, Y. Silver Iodide Formation in Methyl Ammonium Lead Iodide Perovskite Solar Cells with Silver Top Electrodes. *Adv. Mater. Interfaces* **2015**, *2* (13), 2–7.

(41) Liu, X.; Yang, H.; Dai, H.; Mao, X.; Liang, Z. A Novel Photoelectrocatalytic Approach for Water Splitting by an I-BiOCl/Bipolar Membrane Sandwich Structure. *Green Chem.* **2015**, *17* (1), 199–203.

(42) Peedikakkandy, L.; Chatterjee, S.; Pal, A. J. Bandgap Engineering and Efficient Conversion of a Ternary Perovskite (Cs 3 Bi 2 I 9) to a Double Perovskite (Cs 2 NaBiI 6) with the Aid of Alkali Metal Sulfide. *J. Phys. Chem. C* **2020**, *124* (20), 10878–10886.

(43) Li, M.; Xu, S.; Wu, L.; Tang, H.; Zhou, B.; Xu, J.; Yang, Q.; Zhou, T.; Qiu, Y.; Chen, G.; Waterhouse, G. I. N.; Yan, K. Perovskite Cs3Bi2I9 Hexagonal Prisms with Ordered Geometry for Enhanced Photocatalytic Hydrogen Evolution. *ACS Energy Lett.* **2022**, *7* (10), 3370–3377.

(44) Li, W.; Wang, X.; Liao, J.; Jiang, Y.; Kuang, D. Enhanced On–Off Ratio Photodetectors Based on Lead-Free Cs 3 Bi 2 I 9 Single Crystal Thin Films. *Adv. Funct. Mater.* **2020**, *30* (12), 1–9.

(45) Zhang, Y.; Yin, J.; Parida, M. R.; Ahmed, G. H.; Pan, J.; Bakr, O. M.; Brédas, J. L.; Mohammed, O. F. Direct-Indirect Nature of the Bandgap in Lead-Free Perovskite Nanocrystals. *J. Phys. Chem. Lett.* **2017**, *8* (14), 3173–3177.

(46) Fang, H. H.; Adjokatse, S.; Shao, S.; Even, J.; Loi, M. A. Long-Lived Hot-Carrier Light Emission and Large Blue Shift in Formamidinium Tin Triiodide Perovskites. *Nat. Commun.* **2018**, *9* (1).

(47) Manser, J. S.; Kamat, P. V. Band Filling with Free Charge Carriers in Organometal Halide Perovskites. *Nat. Photonics* **2014**, *8* (9), 737–743.

(48) Shil, S. K.; Wang, F.; Lai, Z.; Meng, Y.; Wang, Y.; Zhao, D.; Hossain, M. K.; Egbo, K. O.; Wang, Y.; Yu, K. M.; Ho, J. C. Crystalline All-Inorganic Lead-Free Cs3Sb2I9 Perovskite Microplates with Ultra-Fast Photoconductive Response and Robust Thermal Stability. *Nano Res.* **2021**, *14* (11), 4116–4124.

(49) Pradhan, J.; Das, A.; Panda, A.; Biswas, K. Curious Case of CsPb2Br5: Extremely Soft Structure-Induced Broadband Emission. *Chem. Mater.* **2024**, *36* (7), 3405–3416.

(50) Steele, J. A.; Puech, P.; Keshavarz, M.; Yang, R.; Banerjee, S.; Debroye, E.; Kim, C. W.; Yuan, H.; Heo, N. H.; Vanacken, J.; Walsh, A.; Hofkens, J.; Roeffaers, M. B. J. Giant Electron-Phonon Coupling and Deep Conduction Band Resonance in Metal Halide Double Perovskite. *ACS Nano* **2018**, *12* (8), 8081–8090.

(51) Yang, G.; Tu, Y.; Ye, J.; Liu, R.; Zang, Y.; Zhang, L.; Wang, Y.; Li, G.; Zhou, Q.; Chu, L.; Yan, W. Study on Carrier Dynamics of Perovskite Solar Cells via Transient Absorption. *J. Alloys Compd.* **2023**, *952*, 170051.

(52) Chan, C. C. S.; Fan, K.; Wang, H.; Huang, Z.; Novko, D.; Yan, K.; Xu, J.; Choy, W. C. H.; Lončarić, I.; Wong, K. S. Uncovering the Electron-Phonon Interplay and Dynamical Energy-Dissipation Mechanisms of Hot Carriers in Hybrid Lead Halide Perovskites. *Adv. Energy Mater.* **2021**, *11* (9), 2003071.

(53) Hossain, M.; Sheikh, M. S.; Rao, K. D. M. Hot-Spin Casting Synthesis of Freestanding Cs 2 AgBiBr 6 Double Perovskite Facet-Oriented Microcrystals for Efficient Photodetectors. *Adv. Mater. Interfaces* **2021**, *8* (18), 1–10.

(54) Hossain, M.; Kumar, G. S.; Barimar Prabhava, S. N.; Sheerin, E. D.; McCloskey, D.; Acharya, S.; Rao, K. D. M.; Boland, J. J. Transparent, Flexible Silicon Nanostructured Wire Networks with Seamless Junctions for High-Performance Photodetector Applications. *ACS Nano* **2018**, *12* (5), 4727–4735.

(55) Rao, K. D. M.; Hossain, M.; Umesh; Roy, A.; Ghosh, A.; Kumar, G. S.; Moitra, P.; Kamilya, T.; Acharya, S.; Bhattacharya, S. Transparent, Flexible MAPbI 3 Perovskite Microwire Arrays Passivated with Ultra-Hydrophobic Supramolecular Self-Assembly for Stable and High-Performance Photodetectors. *Nanoscale* **2020**, *12* (22), 11986–11996.

(56) Li, M.; He, Y.; Feng, X.; Qu, W.; Wei, W.; Yang, B.; Wei, H. Reductant Engineering in Stable and High-Quality Tin Perovskite Single Crystal Growth for Heterojunction X-Ray Detectors. *Adv. Mater.* **2023**, *35* (48), 2307042.

(57) Zhou, Y.; Chen, J.; Bakr, O. M.; Mohammed, O. F. Metal Halide Perovskites for X-Ray Imaging Scintillators and Detectors. *ACS Energy Lett.* **2021**, *6* (2), 739–768.

(58) Tie, S.; Zhao, W.; Xin, D.; Zhang, M.; Long, J.; Chen, Q.; Zheng, X.; Zhu, J.; Zhang, W. Robust Fabrication of Hybrid Lead-Free Perovskite Pellets for Stable X-ray Detectors with Low Detection Limit. *Adv. Mater.* **2020**, *32* (31), 1–7.

(59) Xu, Z.; Liu, X.; Li, Y.; Liu, X.; Yang, T.; Ji, C.; Han, S.; Xu, Y.; Luo, J.; Sun, Z. Exploring Lead-Free Hybrid Double Perovskite Crystals of (BA) 2 CsAgBiBr 7 with Large Mobility-Lifetime Product toward X-Ray Detection. *Angew. Chemie Int. Ed.* **2019**, *58* (44), 15757–15761.

(60) Xia, M.; Yuan, J.; Niu, G.; Du, X.; Yin, L.; Pan, W.; Luo, J.; Li, Z.; Zhao, H.; Xue, K.; Miao, X.; Tang, J. Unveiling the Structural Descriptor of A 3 B 2 X 9 Perovskite Derivatives toward X-Ray Detectors with Low Detection Limit and High Stability. *Adv. Funct. Mater.* **2020**, *30* (24), 2–9.

(61) Sun, Q.; Xu, Y.; Zhang, H.; Xiao, B.; Liu, X.; Dong, J.; Cheng, Y.; Zhang, B.; Jie, W.; Kanatzidis, M. G. Optical and Electronic Anisotropies in Perovskitoid Crystals of Cs3 Bi2I9 Studies of Nuclear Radiation Detection. *J. Mater. Chem. A* **2018**, *6* (46), 23388–23395.

(62) Bu, N.; Jia, S.; Xiao, Y.; Li, H.; Li, N.; Liu, X.; Yang, Z.; Zhao, K.; Liu, S. (Frank). Inch-Size Cs3Bi2I9 Polycrystalline Wafers with near-Intrinsic Properties for Ultralow-Detection-Limit X-Ray Detection. *J. Mater. Chem. C* **2022**, *10* (17), 6665–6672.

(63) Li, X.; Zhang, P.; Hua, Y.; Cui, F.; Sun, X.; Liu, L.; Bi, Y.; Yue, Z.; Zhang, G.; Tao, X. Ultralow Detection Limit and Robust Hard X-Ray Imaging Detector Based on Inch-Sized Lead-Free Perovskite Cs3Bi2Br9 Single Crystals. *ACS Appl. Mater. Interfaces* **2022**, *14* (7), 9340–9351.

(64) Leng, M.; Yang, Y.; Zeng, K.; Chen, Z.; Tan, Z.; Li, S.; Li, J.; Xu, B.; Li, D.; Hautzinger, M. P.; Fu, Y.; Zhai, T.; Xu, L.; Niu, G.; Jin, S.; Tang, J. All-Inorganic Bismuth-Based Perovskite Quantum Dots with Bright Blue Photoluminescence and Excellent Stability. *Adv. Funct. Mater.* **2018**, *28* (1), 1704446.

(65) Liu, Y.; Xu, Z.; Yang, Z.; Zhang, Y.; Cui, J.; He, Y.; Ye, H.; Zhao, K.; Sun, H.; Lu, R.;

Liu, M.; Kanatzidis, M. G.; Liu, S. (Frank). Inch-Size 0D-Structured Lead-Free Perovskite Single Crystals for Highly Sensitive Stable X-Ray Imaging. *Matter* **2020**, *3* (1), 180–196.

(66) Daum, M.; Deumel, S.; Sytnyk, M.; Afify, H. A.; Hock, R.; Eigen, A.; Zhao, B.; Halik, M.; These, A.; Matt, G. J.; Brabec, C. J.; Tedde, S. F.; Heiss, W. Self-Healing Cs3Bi2Br3I6 Perovskite Wafers for X-Ray Detection. *Adv. Funct. Mater.* **2021**, *31* (47), 2102713.

(67) Xia, M.; Yuan, J.-H.; Niu, G.; Du, X.; Yin, L.; Pan, W.; Luo, J.; Li, Z.; Zhao, H.; Xue, K.-H.; Miao, X.; Tang, J. Unveiling the Structural Descriptor of A3B2X9 Perovskite Derivatives toward X-Ray Detectors with Low Detection Limit and High Stability. *Adv. Funct. Mater.* **2020**, *30* (24), 1910648.

(68) Dudipala, K. R.; Le, T.; Nie, W.; Hoye, R. L. Z. Halide Perovskites and Their Derivatives for Efficient, High-Resolution Direct Radiation Detection: Design Strategies and Applications. *Adv. Mater.* **2023**, 2304523.

(69) Sarkar, A.; Acharyya, P.; Sasmal, R.; Pal, P.; Agasti, S. S.; Biswas, K. Synthesis of Ultrathin Few-Layer 2D Nanoplates of Halide Perovskite Cs3Bi2I9 and Single-Nanoplate Super-Resolved Fluorescence Microscopy. *Inorg. Chem.* **2018**, *57* (24), 15558–15565.

(70) Jubu, P. R.; Yam, F. K.; Igba, V. M.; Beh, K. P. Tauc-Plot Scale and Extrapolation Effect on Bandgap Estimation from UV–Vis–NIR Data – A Case Study of β-Ga2O3. *J. Solid State Chem.* **2020**, *290* (July), 121576.

(71) Wang, V.; Xu, N.; Liu, J.-C.; Tang, G.; Geng, W.-T. VASPKIT: A User-Friendly Interface Facilitating High-Throughput Computing and Analysis Using VASP Code. *Comput. Phys. Commun.* **2021**, *267*, 108033.

(72) D. Whalley, L. Effmass: An Effective Mass Package. *J. Open Source Softw.* **2018**, *3* (28), 797.

Entry for the Table of Contents